

---

# RESViT: RESIDUAL VISION TRANSFORMERS FOR MULTI-MODAL MEDICAL IMAGE SYNTHESIS

---

A PREPRINT

**Onat Dalmaz<sup>1,2</sup>, Mahmut Yurt<sup>1,2</sup>, Tolga Çukur<sup>1,2,3</sup>**

<sup>1</sup> Department of Electrical and Electronics Engineering, Bilkent University, Ankara 06800, Turkey

<sup>2</sup> National Magnetic Resonance Research Center (UMRAM), Bilkent University, Ankara 06800, Turkey

<sup>3</sup> Neuroscience Program, Bilkent University, Ankara 06800, Turkey

July 1, 2021

## ABSTRACT

Multi-modal imaging is a key healthcare technology in the diagnosis and management of disease, but it is often underutilized due to costs associated with multiple separate scans. This limitation yields the need for synthesis of unacquired modalities from the subset of available modalities. In recent years, generative adversarial network (GAN) models with superior depiction of structural details have been established as state-of-the-art in numerous medical image synthesis tasks. However, GANs are characteristically based on convolutional neural network (CNN) backbones that perform local processing with compact filters. This inductive bias, in turn, compromises learning of long-range spatial dependencies. While attention maps incorporated in GANs can multiplicatively modulate CNN features to emphasize critical image regions, their capture of global context is mostly implicit. Here, we propose a novel generative adversarial approach for medical image synthesis, ResViT, to combine local precision of convolution operators with contextual sensitivity of vision transformers. Based on an encoder-decoder architecture, ResViT employs a central bottleneck comprising novel aggregated residual transformer (ART) blocks that synergistically combine convolutional and transformer modules. Comprehensive demonstrations are performed for synthesizing missing sequences in multi-contrast MRI and CT images from MRI. Our results indicate the superiority of ResViT against competing methods in terms of qualitative observations and quantitative metrics.

**Keywords** medical image synthesis · transformer · adversarial · generative · residual · multimodal · image-to-image translation · unified

## 1 Introduction

Medical imaging plays a pivotal role in modern healthcare by enabling *in vivo* examination of pathology in the human body. In many clinical scenarios, multi-modal protocols are desirable that involve a diverse collection of images from multiple scanners (e.g., CT, MRI, PET) [1], or multiple acquisitions from a single scanner (multi-contrast MRI) [2]. Complementary information about tissue morphology, in turn, empower physicians to diagnose with higher accuracy and confidence. Unfortunately, numerous factors including uncooperative patients and excessive scan times, prohibit ubiquitous multi-modal imaging [3,4]. As a result, there has been ever-growing interest in synthesizing unacquired images in multi-modal protocols from the subset of available images, bypassing costs associated with additional scans [5,6].

Medical image synthesis aims to predict target-modality images for a subject given source-modality images acquired under a limited scan budget. This is an ill-posed inverse problem since medical images are high dimensional and there are stark differences in tissue contrast across modalities [7]. Two fundamental solutions to this problem are atlas-based registration methods [8–13], and voxel-intensity transformations [14–21]. Registration methods perform synthesis via

a geometric mapping between the anatomical space of the test subject and a multi-modal atlas, so they offer limited sensitivity in capturing subject-specific patterns [8–11]. Intensity-transformation methods instead cast synthesis as a nonlinear mapping between source-target modalities [14, 16, 18, 20, 21]. Since data are left in anatomical spaces of individual subjects, these methods are better suited to preserve idiosyncratic anatomy.

In recent years, the imaging field has witnessed a major overhaul with rapid adoption of deep learning for intensity-based source-to-target mapping. Learning-based synthesis performs mapping with neural network models, which are trained on databases of source-target images [22–28]. Earlier efforts in this domain reported that convolutional neural network (CNN) architectures yield significant performance improvements over non-network-based approaches [22–24, 29–31]. CNN models are primarily trained to minimize pixel-wise losses (e.g., mean-absolute error or mean-squared error) between synthetic and ground truth images [22, 23, 31]. Pixel-wise losses tend to over-emphasize low spatial frequencies, so they perform poorly in higher frequencies [25, 32]. To alleviate high-frequency errors in synthetic images, generative adversarial networks (GAN) were later introduced [25–28, 33–45]. GAN models involve an adversarial loss that sets up a game-theoretic interplay between generator and discriminator networks to substantially improve capture of detailed tissue structure [26, 27, 39].

Despite their prowess, GAN models offering state-of-the-art performance in many synthesis tasks are based on convolutional architectures [25, 32, 46]. Convolutional layers perform local processing via compact filters trained to minimize image-averaged loss terms. Therefore, CNNs have limited ability to cope with atypical anatomy showing large across-subject variability [47], and to learn long-range spatial dependencies between distant regions [48]. To guide focus towards critical image regions, recent studies have proposed self-attention GAN models leveraging spatial and channel attention mechanisms [49–52]. While such attention maps induce multiplicative modulation of CNN features to emphasize critical information [53], they do not explicitly model long-range dependencies. In contrast, the emergent Transformer architectures in natural language processing and computer vision forego convolution altogether in favor of intrinsic global attention operators [51, 54–56]. That said, the adoption of pure Transformer architectures in imaging tasks with pixel-level outputs is challenging due to their computational burden and limited localization abilities [56].

Here, we propose a novel deep learning model for medical image synthesis, ResViT, that combines the sensitivity of vision transformers to global context, the localization power of CNNs, and the realism of adversarial learning. ResViT’s generator follows an encoder-decoder architecture with a central bottleneck to distill task-critical information. The encoder and decoder comprise residual CNN blocks to leverage inductive bias and local precision of convolution operators [57]. The information bottleneck comprises novel aggregated residual transformer (ART) blocks inserted at key locations within the residual pathway to synergistically preserve local and global context, with a weight-sharing strategy to minimize model complexity. To improve practical utility, a unified ResViT implementation is introduced that consolidates synthesis models for numerous configurations of source-target modalities. ResViT is compared against state-of-the-art synthesis models including CNN-based GANs (pix2pix [32], pGAN [25], MM-GAN [28]), self-attention GANs (Attention U-Net [58], SAGAN [53]), and a recent transformer-based architecture (TransUNet [47]). Comprehensive demonstrations are performed in many-to-one and one-to-one tasks to synthesize missing sequences in multi-contrast MRI and to recover CT from MRI. Our experiments clearly indicate the superiority of the proposed method against competing methods in all medical image synthesis tasks.

## Contributions

- We introduce the first adversarial model for medical image synthesis that incorporates transformers in a residual generator network.
- The proposed model comprises novel aggregated residual transformer (ART) blocks in an information bottleneck to synergistically preserve localization and context.
- We introduce a weight sharing strategy among ART blocks to lower model complexity and mitigate computational burden.
- We introduce a unified synthesis model that generalizes across multiple configurations of source-target modalities.
- We provide demonstrations on both one-to-one and many-to-one synthesis tasks, where ResViT outperforms state-of-the-art CNN-based and transformer architectures for medical imaging.

## 2 Related Work

The immense success of deep learning in inverse problem solutions has motivated its rapid adoption in medical imaging [59, 60]. Medical image synthesis is an overtly ill-posed problem given that no data samples are collected on the to-be-predicted target modality [45]. Therefore, synthesizing an unavailable target modality from acquired source

modalities has significantly benefited from learning-based methods. Earlier studies in this domain have proposed local networks based on patch-level processing [16, 61, 62]. While patch-level network models offer elevated performance over traditional synthesis approaches, they can potentially show limited sensitivity to broader context across images [23]. Later studies adopted deep CNN architectures for image-level processing, thanks to the increasing availability of large imaging databases and effective training strategies to permit more complex models. CNN-based synthesis has been successfully demonstrated in various applications including synthesis across MR scanners [45, 63–65], multi-contrast MR synthesis [22–24, 29–31], and CT synthesis [66–69]. Despite the significant performance improvements they enable, CNN models trained with pixel-wise loss terms such as mean-absolute error or mean-squared error tend to suffer from undesirable loss of detailed structure in target images [25, 32, 46].

To improve capture of structural details in synthetic images, GAN [33] architectures were proposed to learn the probability distribution of target modalities conditioned on source modalities [70]. Adversarial loss terms empower GAN models to capture a prior for target images and thereby improve recovery of high-spatial-resolution information [25, 32, 46]. In recent years, GAN-based methods were demonstrated to offer state-of-the-art performance in numerous medical image synthesis tasks, including data augmentation as well as multi-modal synthesis [25, 27, 71, 72]. Among important applications are CT to PET synthesis [73, 74], MR to CT synthesis [75–77], unpaired cross-modality synthesis [78–81], 3T-to-7T synthesis [82, 83], and multi-contrast MRI synthesis [25–28, 34–37, 39–42, 44, 45].

While GAN methods have arguably emerged as a gold standard in recent years, they are not without limitation. In particular, state-of-the-art GAN models are based on purely convolutional operators that are known to suffer from poor across-subject generalization to atypical anatomy and sub-optimal learning of long-range spatial dependencies [47]. Recent studies have incorporated spatial and channel attention mechanisms to modulate CNN-derived feature maps [36, 53, 58, 84–87]. Such attentional modulation motivates the network to give greater focus to regions that may suffer from performance losses [53, 58]. While attention maps might be distributed across broad image regions, multiplicative gating of local CNN features only offers implicit modeling of global context [47, 88].

To explicitly incorporate contextual representations, recent studies have considered hybrid transformer-CNN architectures or full transformer architectures for medical image segmentation and disease classification [88–93]. Closest to our work are few independent efforts in medical image synthesis. [89] used transformers for retinal image synthesis, [90] included a transformer in the discriminator of a UNet-based GAN for MR-to-PET synthesis, and [91] used a non-adversarial UNet-based performer architecture for one-to-one MRI synthesis in infant brains. Differently from these recent efforts, here we introduce an adversarial transformer architecture inspired by the powerful ResNet model [25, 57]. Novel aggregated residual transformer (ART) blocks are injected in the information bottleneck of the generator in ResViT. Our hybrid CNN-transformer approach consolidates the localization power of convolutional representations with the contextual abilities of transformers. Furthermore, we provide the first demonstrations of a transformer architecture for many-to-one synthesis tasks and a unified synthesis model for advancing practicality over existing methods.

### 3 Theory

#### 3.1 Residual Vision Transformers

Here we propose a novel adversarial framework for multi-modal medical image synthesis named residual vision transformers, ResViT. ResViT is a conditional image synthesis model that unifies various source-target modality configurations into a single model for improved practicality. To do this, it leverages a hybrid adversarial architecture of deep convolutional operators and attention-based residual transformer blocks to simultaneously learn high-resolution structural and global contextual features (Fig. 1). The proposed architecture follows an encoder - information bottleneck - decoder pathway in the generator subnetwork, where the bottleneck contains a stack of residual blocks to distill structural and contextual representations. Meanwhile, the discriminator subnetwork is composed of deep convolutional operators. In the remainder of this section, we explain the detailed composition of each network component, and we describe the loss functions to train ResViT for unified image synthesis.

**Encoder** The first component of ResViT is a deep encoder network that contains a series of convolutional layers to capture a hierarchy of localized features of source images. Note that ResViT is a unified synthesis model, so its encoder receives as input the full set of modalities within the multi-modal imaging protocol, including both source and target modalities (Fig. 2). Source modalities are input via an identity mapping, whereas target modalities are masked out:

$$X_i^G = a_i (\mathbf{1} \cdot m_i) + (1 - a_i) (\mathbf{0} \cdot m_i) \quad (1)$$

where  $i$  denotes the channel index of the encoder input where  $i \in \{1, 2, \dots, I\}$ ,  $m_i$  denotes the images for the  $i$ th modality,  $\mathbf{0}$  denotes a tensor of zeros, and  $\mathbf{1}$  denotes a tensor of ones. In Eq. (1),  $a_i$  denotes the availability of the  $i$ th

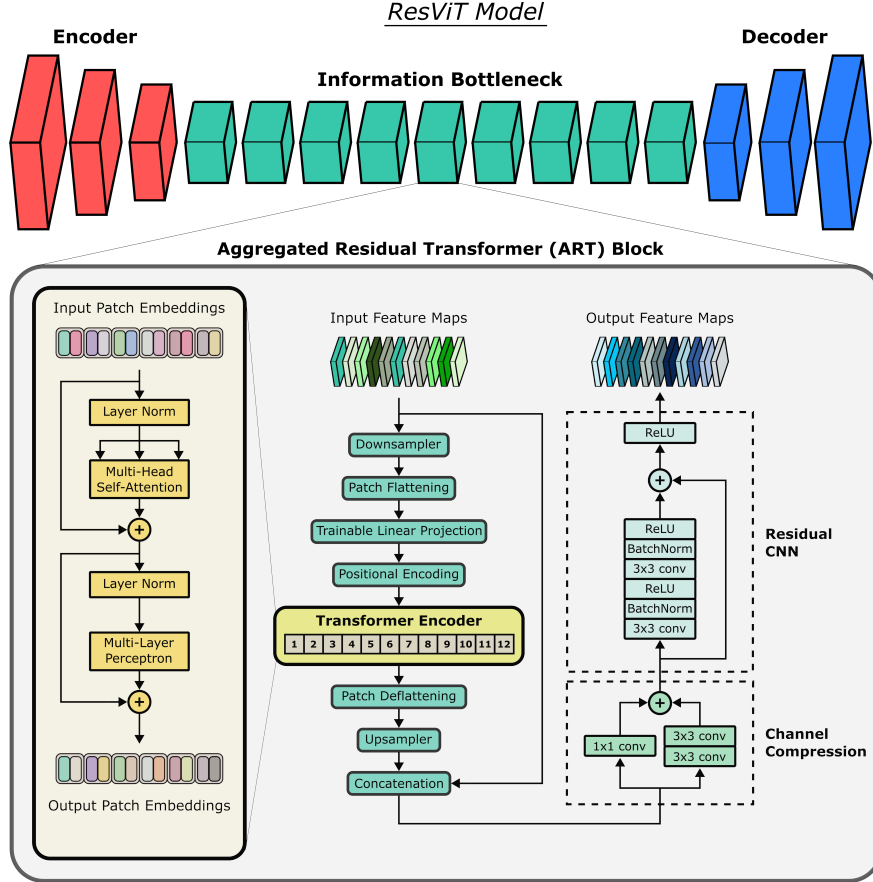


Figure 1: The generator in ResViT follows an encoder-decoder architecture bridged with a central information bottleneck to distill task-specific information. The encoder and decoder comprise convolutional layers to maintain local precision and inductive bias in learned structural representations. Meanwhile, the information bottleneck comprises a stack of novel aggregated residual transformer (ART) blocks. ART blocks learn contextual representations via vision transformers, and synergistically fuse CNN-based local and transformer-based global representations.

modality:

$$a_i = \begin{cases} 1 & \text{if } m_i \text{ is a source modality} \\ 0 & \text{if } m_i \text{ is a target modality} \end{cases} \quad (2)$$

During training, various different configurations of source and target modalities are considered within the multi-modal protocol (e.g.,  $T_1, T_2 \rightarrow PD$ ;  $T_2, PD \rightarrow T_1$ ;  $T_1, PD \rightarrow T_2$  for a three contrast MRI protocol). During inference, the specific source-target configuration is determined via the availability conditions in individual test subjects. Given the availability-masked multi-channel input, the encoder uses convolutional operators to learn latent structural representations shared across the consolidated synthesis tasks:

$$encoder(X^G) = f_{n_e} \in \mathbb{R}^{N_C, H, W} \quad (3)$$

where  $f_{n_e}$  is the embedded latent tensor after  $n_e$  network layers of the encoder,  $N_C$  denotes the number channels,  $H$  denotes the height, and  $W$  denotes the width of the tensor. The resulting representations are then fed to the information bottleneck.

**Information Bottleneck** Next, ResViT employs a residual bottleneck to distill task-relevant information in the encoded image features. Note that convolution-based operators in CNNs have greater power in capturing localized features, whereas attention-based operators in transformers are more sensitive to context-driven features. To simultaneously maintain localization power and contextual sensitivity, we propose to use novel aggregated residual transformer (ART) blocks in ResViT.

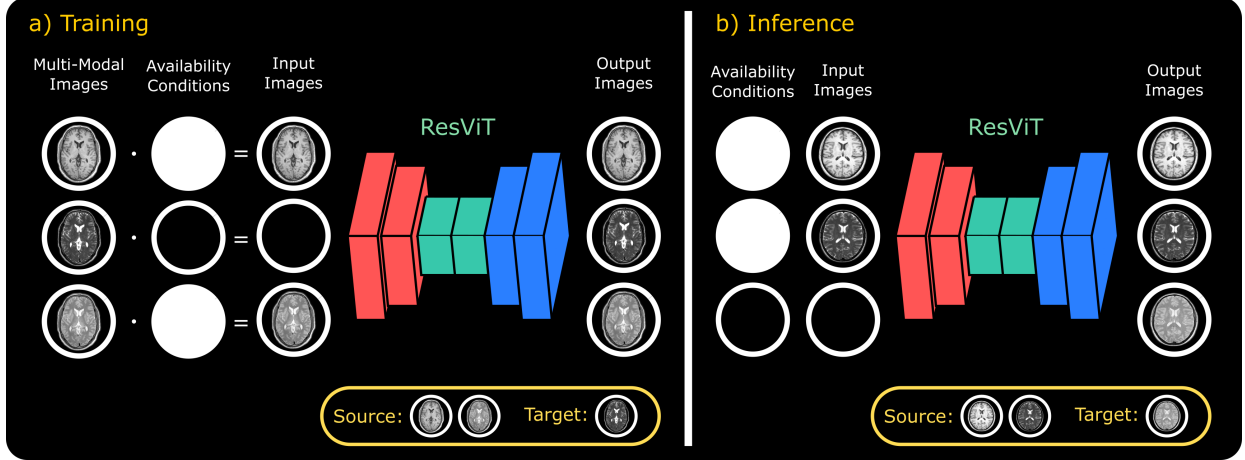


Figure 2: ResViT is a conditional image synthesis model that unifies various source-target modality configurations into a single model for improved practicality. a) During training, ResViT takes as input the entire set of images within the multi-modal protocol, including both source and target modalities. For model consolidation across multiple synthesis tasks, various configurations of source-target modalities are expressed in terms of availability conditions in ResViT. b) During inference, the specific source-target configuration is determined via the availability conditions in each given test subject.

The main function of ART blocks is to aggregate the information distilled via residual convolutional and transformer branches (Fig. 1). Receiving as input the  $j$ th layer feature maps denoted as  $f_j \in \mathbb{R}^{N_C, H, W}$ , an ART block first processes the feature maps via a visual transformer. Note that, given computational constraints, the vision transformer expects feature maps at smaller resolutions compared to convolutional layers. Thus, the spatial dimensions ( $H, W$ ) of  $f_j \in \mathbb{R}^{N_C, H, W}$  are lowered by a downsampling block  $\mathbf{DS}$ :

$$f'_j \in \mathbb{R}^{N'_C, H', W'} = \mathbf{DS}(f_j) \quad (4)$$

where  $\mathbf{DS}$  is implemented as a stack of strided convolutional layers,  $f'_j \in \mathbb{R}^{N'_C, H', W'}$  denotes the downsampled feature maps with  $W' = W/M$ , and  $H' = H/M$  where  $M$  denotes the downsampling factor. A vision transformer branch then processes  $f'_j$  to extract contextual information. Here, the transformer branch is implemented based on the recently introduced vision transformer model (ViT) [56]. Accordingly,  $f'_j$  is first split into non-overlapping patches of size  $(P, P)$ , and the patches are then flattened:

$$f_j^1 = \text{flatten}(f'_j[:, 1:P, 1:P]) \quad (5)$$

$$f_j^2 = \text{flatten}(f'_j[:, P+1:2P, 1:P]) \quad (6)$$

$$\vdots \quad (7)$$

$$f_j^{N_P} = \text{flatten}(f'_j[:, H' - P:H', W' - P:W']) \quad (8)$$

where  $f_j^p \in \mathbb{R}^{N'_C P^2}$  denotes the  $p$ th patch where  $p \in \{1, 2, \dots, N_P\}$ , and  $N_P = W' H' / P^2$  denotes the number of flattened patches. The transformer embeds flattened image patches onto an  $N_D$ -dimensional space via trainable linear projections, supplemented with learnable positional encodings:

$$z_0 = [f_j^1 P_E; f_j^2 P_E; \dots; f_j^{N_P} P_E] + P_E^{pos} \quad (9)$$

where  $z_0 \in \mathbb{R}^{N_P, N_D}$  denotes patch embeddings that the transformer encoder takes as input,  $P_E$  is the embedding projection, and  $P_E^{pos}$  is the learnable positional embedding that carries information about patch location.

Next, the transformer encoder processes the patch embeddings via a cascade of  $L$  layers of multi-head self-attention (**MSA**) and multi-layer perceptrons (**MLP**). The output of the  $l$ th layer in the transformer encoder is thereby expressed as:

$$z'_l = \mathbf{MSA}(\mathbf{LN}(z_{l-1})) + z_{l-1} \quad (10)$$

$$z_l = \mathbf{MLP}(\mathbf{LN}(z'_l)) + z'_l \quad (11)$$

In Eq. 7,  $\mathbf{LN}$  stands for layer normalization:

$$z_l^{LN} = \mathbf{LN}(z_l) = \frac{z_l - \mu}{\sqrt{\sigma^2 + \epsilon}} \quad (12)$$

where  $\epsilon$  is a small number preventing from division by zero, and  $\mu$ - $\sigma$  are formulated as:

$$\mu = \frac{1}{N_D} \sum_{d=1}^{N_D} z_l(d), \quad \sigma = \sqrt{\frac{1}{N_D} \sum_{d=1}^{N_D} (z_l(d) - \mu)^2} \quad (13)$$

Meanwhile,  $\mathbf{MSA}$  layers in Eq. 8 employ  $S$  separate self-attention  $\mathbf{SA}$  heads:

$$\mathbf{MSA}(z) = [\mathbf{SA}_1(z); \mathbf{SA}_2(z); \dots; \mathbf{SA}_S(z)]U_{msa} \quad (14)$$

where  $\mathbf{SA}_s$  stands for the  $s$ th attention head where  $s \in \{1, 2, \dots, S\}$  and  $U_{msa}$  denotes the learnable tensor projecting attention head outputs.  $\mathbf{SA}$  layers compute a weighted combination of all elements of the input sequence  $z$ :  $\mathbf{SA}(z) = Av$  where attention weights  $A_{a,b}$  are taken as pairwise similarity between the query  $q$  and key  $k$ :

$$A_{a,b} = \text{softmax}(q_a k_b^T / N_D^{0.5}) \quad (15)$$

The output of the transformer encoder  $z_L$  is then deflattened for the subsequent convolutional operations:

$$g'_j[:, 1 : P, 1 : P] = \text{deflatten}(z_L[1]) \quad (16)$$

$$g'_j[:, P + 1 : 2P, 1 : P] = \text{deflatten}(z_L[2]) \quad (17)$$

$$\vdots \quad (18)$$

$$g'_J[:, H' - P : H', W' - P : W'] = \text{deflatten}(z_L[N_P]) \quad (19)$$

where  $g'_j \in \mathbb{R}^{N_D, H', W'}$  denotes the deflattened feature map tensor.  $\mathbf{US}$  block is implemented as a cascade of transposed convolutional layers. The resolution of  $g'_j$  is increased to match the size of the input feature maps via an upsampling block  $\mathbf{US}$ :

$$g_j \in \mathbb{R}^{N_C, H, W} = \mathbf{US}(g'_j) \quad (20)$$

where  $g_j \in \mathbb{R}^{N_C, H, W}$  denotes the upsampled feature maps that the vision transformer module produces as output. The global context learned via the vision transformer is then fused with the localized features captured with convolutional operators:

$$h'_j \in \mathbb{R}^{2N_C, H, W} = \text{concat}(f_j, g_j) \quad (21)$$

where  $h'_j$  denotes the concatenated feature maps.

To maintain a fixed tensor size across ART blocks, the channels of the concatenated feature maps are then compressed via a channel compression block:

$$h_j \in \mathbb{R}^{N_C, H, W} = \mathbf{CC}(h'_j) \quad (22)$$

where  $\mathbf{CC}$  stands for the channel compression block, and  $h_j$  denotes the compressed feature maps. Here,  $\mathbf{CC}$  is implemented as two shunt-connected convolutional branches of varying kernel size. Finally, the feature maps are processed via a residual CNN ( $\mathbf{ResCNN}$ ) to distill learned structural and contextual representations:

$$f_{j+1} \in \mathbb{R}^{N_C, H, W} = \mathbf{ResCNN}(h_j) \quad (23)$$

where  $f_{j+1}$  denotes the output of the ART block at the  $j$ th network layer.

**Decoder** The last component of ResViT’s generator is a deep decoder network that contains a series of convolutional layers. Because ResViT is a unified synthesis model, its decoder synthesizes all contrasts within the multi-modal protocol regardless of the specific source-target configuration (Fig. 2). The decoder receives as input the feature maps distilled by the information bottleneck and produces multi-modality images in separate channels:

$$\hat{Y}^G = \text{decoder}(f_{n_e+n_i}) \quad (24)$$

where  $f_{n_e+n_i}$  denotes the output of the last ART block,  $n_e$  denotes the number of layers in the encoder,  $n_i$  denotes the number of layers in the information bottleneck, and  $\hat{Y}_i^G \in \hat{Y}^G$  denotes the  $i$ th synthesized modality.

**Parameter Sharing Transformers** Multiple ART blocks are used in the information bottleneck to increase the capacity of ResViT in learning complex contextual representations. That said, multiple independent transformer blocks would inevitably elevate memory demand and risk of overfitting due to an excessive number of parameters. To prevent these risks, a weight-sharing strategy is adopted across ART blocks to maintain low model complexity.

**Discriminator** The discriminator in the adversarial ResViT model is based on a conditional PatchGAN architecture [32]. The discriminator performs patch-level differentiation between acquired medical images and synthetic images produced by the generator. This patch-based implementation increases sensitivity to localized details related to high-spatial-frequency information. As ResViT is a unified model with a decoder that generates all modalities in the multi-modal protocol including source modalities, an availability-guided selective discriminator is employed:

$$X_i^D(\text{source}) = X_i^G = a_i(\mathbf{1} \cdot m_i) + (1 - a_i)\mathbf{0} \quad (25)$$

$$X_i^D(\text{syn target}) = (1 - a_i)(\mathbf{1} \cdot Y_i^G) + a_i\mathbf{0} \quad (26)$$

$$X_i^D(\text{acq target}) = (1 - a_i)(\mathbf{1} \cdot m_i) + a_i\mathbf{0} \quad (27)$$

$$(28)$$

where  $X_i^D(\text{source})$  denotes the source images,  $X_i^D(\text{syn target})$  denotes the synthesized target images, and  $X_i^D(\text{acq target})$  denotes the acquired target images. Here, the input to the conditional discriminator is the concatenation of source and target images:

$$X^D(\text{synthetic}) = \text{concat}(X_i^D(\text{source}), X_i^D(\text{syn target})) \quad (29)$$

$$X^D(\text{acquired}) = \text{concat}(X_i^D(\text{source}), X_i^D(\text{acq target})) \quad (30)$$

where  $X^D(\text{synthetic})$  is the concatenation of the source and synthetic target images and  $X^D(\text{acquired})$  is the concatenation of the source and acquired target images.

**Loss Function** The first component of the loss function in the ResViT model is a pixel-wise  $L_1$  loss that is defined between the acquired and synthesized target modalities:

$$L_{pix} = \sum_{i=1}^I (1 - a_i) \mathbb{E}[||G(X^G)_i - m_i||_1] \quad (31)$$

where  $\mathbb{E}$  denotes expectation, and  $G$  denotes the generator submodule in the ResViT architecture comprising the encoder, information bottleneck and decoder. The second component of the loss function is a pixel-wise reconstruction loss between the acquired and reconstructed source modalities based on an  $L_1$  distance:

$$L_{rec} = \sum_{i=1}^I a_i \mathbb{E}[||G(X^G)_i - m_i||_1] \quad (32)$$

The last component of the loss function in ResViT is an adversarial loss function that is defined via the conditional discriminator:

$$L_{adv} = -\mathbb{E}[D(X^D(\text{acquired}))^2] - \mathbb{E}[(D(X^D(\text{synthetic})) - 1)^2] \quad (33)$$

$$(34)$$

where  $D$  denotes the conditional discriminator,  $X^D(\text{synthetic})$  is the concatenation of the source and synthetic target images, and  $X^D(\text{acquired})$  is the concatenation of the source and acquired target images. Finally, the loss functions are linearly combined to form the overall objective as follows:

$$L_{ResViT} = \lambda_{pix} L_{pix} + \lambda_{rec} L_{rec} + \lambda_{adv} L_{adv} \quad (35)$$

where  $\lambda_{pix}$  denotes the weighing of the pixel-wise loss,  $\lambda_{rec}$  denotes the weighing of the reconstruction loss, and  $\lambda_{adv}$  denotes the weighing of the adversarial loss.

## 4 Methods

### 4.1 Datasets

We demonstrated the proposed ResViT model on two multi-contrast brain MRI datasets (IXI: <https://brain-development.org/ixi-dataset/>, BRATS [94–96] and a multi-modal pelvic MRI-CT dataset [97]). Details regarding each dataset are given below:

**IXI Dataset**  $T_1$ -weighted,  $T_2$ -weighted, and PD-weighted brain MR images from 53 healthy subjects were analyzed. 25 subjects were reserved for training, 10 were reserved for validation, and 18 were reserved for testing. From each subject, 100 axial cross-sections containing brain tissues were selected. Acquisition parameters were as follows.  $T_1$ -weighted images:  $TE = 4.603ms$ ,  $TR = 9.813ms$ , spatial resolution =  $0.94 \times 0.94 \times 1.2mm^3$ .  $T_2$ -weighted images:  $TE = 100ms$ ,  $TR = 8178.34ms$ , spatial resolution =  $0.94 \times 0.94 \times 1.2mm^3$ . PD-weighted images:  $TE = 8ms$ ,  $TR = 8178.34ms$ , spatial resolution =  $0.94 \times 0.94 \times 1.2mm^3$ . The multi-contrast images in this dataset were unregistered. Hence,  $T_2$ - and PD-weighted images were spatially registered onto  $T_1$ -weighted images prior to modelling. Registration was performed via an affine transformation in FSL [98] based on mutual information.

**BRATS Dataset**  $T_1$ -weighted,  $T_2$ -weighted, post-contrast  $T_2$ -weighted, and  $T_2$  Fluid Attenuation Inversion Recovery (FLAIR) brain MR images from 55 subjects were analyzed. 25 subjects were reserved for training, 10 were reserved for validation, and 20 were reserved for testing. From each subject, 100 axial cross-sections containing brain tissues were selected. Please note that the BRATS dataset contains images collected under various clinical protocols and scanners at multiple institutions. As publicly shared, multi-contrast images are co-registered to the same anatomical template, interpolated to  $1 \times 1 \times 1mm^3$  resolution and skull-stripped.

**MRI-CT Dataset**  $T_2$ -weighted MR and CT images of the male pelvis from 15 subjects were used. 9 subjects were reserved for training, 2 were reserved for validation, and 4 were reserved for testing. From each subject, 90 axial cross-sections were analysed. Acquisition parameters were as follows.  $T_2$ -weighted MR images: Group 1,  $TE = 97ms$ ,  $TR = 6000 - 6600ms$ , spatial resolution =  $0.875 \times 0.875 \times 2.5mm^3$ . Group 2,  $TE = 91 - 102ms$ ,  $TR = 12000 - 16000ms$ , spatial resolution =  $0.875 - 1.1 \times 0.875 - 1.1 \times 2.5mm^3$ . CT images: Group 1, spatial resolution =  $0.98 \times 0.98 \times 3mm^3$ , Kernel =  $B30f$ . Group 2: spatial resolution =  $0.1 \times 0.1 \times 2mm^3$ , Kernel =  $FC17$ . This MRI-CT dataset contains images collected under various different protocols and scanners for each modality. As publicly shared, multi-modal images are co-registered onto  $T_2$ -weighted MR scans.

## 4.2 Competing Methods

We demonstrated the proposed ResViT model against several state-of-the-art image synthesis methods. Hyperparameters of each competing method were optimized via identical cross-validation procedures. All models were implemented in an adversarial setup.

### 4.2.1 Convolutional GANs

**pGAN:** A convolutional GAN model, pGAN, with ResNet backbone was considered [25]. pGAN comprises CNN-based generator and discriminator networks [25]. Its generator comprises an encoder, bottleneck, and decoder, where the encoder and decoder are identical to those in ResViT. The bottleneck contains a cascade of 9 residual CNN blocks. Note that pGAN receives as input a specific collection of source modality images to synthesize target modality images in one-to-one or many-to-one settings, so a separate pGAN model was trained independently for each distinct synthesis task.

**pix2pix:** A convolutional GAN model, pix2pix, with U-Net backbone was considered [32]. The CNN-based pix2pix has a generator with an encoder-decoder structure tied with skip connections [32]. An independent pix2pix model was learned for each distinct synthesis task.

**MM-GAN:** A unified synthesis model based on a convolutional GAN architecture was considered [28]. MM-GAN comprises CNN-based generator and discriminator networks, where the generator is based on U-Net. MM-GAN trains a single network under various source-target modality configurations. The original MM-GAN architecture was directly adopted, except for curriculum learning to ensure standard sample selection for all competing methods. The unification strategy in MM-GAN matches the unification strategy in ResViT.

**pGAN<sub>uni</sub>:** A unified version of the pGAN model was trained to consolidate multiple synthesis tasks. The unification procedure was identical to that of ResViT.

### 4.2.2 Attention-based GANs

**Attention U-Net GAN (A-UNet):** A CNN-based U-Net architecture with additive attention gates was considered [58]. Here we adopted the original A-UNet model as the generator of a conditional GAN model, where the discriminator was identical to that in ResViT.

**Self-Attention GAN (SAGAN):** A CNN-based GAN model with self-attention modules incorporated into the generator was considered [53]. Here we adapted the original SAGAN model designed for unconditional mapping by inserting the self-attention modules into the pGAN model as described in [99]. For a fair comparison, the number and position of attention modules in SAGAN were matched to those of transformer modules in ResViT. A separate SAGAN model was learned for each distinct synthesis task.

#### 4.2.3 Transformer GANs

**TransUNet GAN:** A hybrid CNN-transformer architecture, TransUNet [47], recently introduced for medical image segmentation, was considered. Here, we adopted the original TransUNet model as the generator of a conditional GAN architecture with an identical discriminator to ResViT. We further replaced the segmentation head with a convolutional layer for synthesis. A separate TransUNet model was trained for each distinct synthesis task.

**TransUNet<sub>uni</sub>:** The TransUNet model was unified to consolidate multiple synthesis tasks. The unification procedure was identical to that of ResViT.

### 4.3 Implementation Details

The encoder in the ResViT model contained three convolutional layers of kernel size 7, 3, 3 respectively. The feature map in the encoder output was of size  $\mathbb{R}^{256, 64, 64}$ , and this dimensionality was retained across the information bottleneck. The decoder contained 3 convolutional layers of kernel size 3, 3, 7 respectively. The information bottleneck contained 9 ART blocks. The downsampling modules preceding transformers contained 2 convolutional layers with stride 2 and kernel size 3. The upsampling modules succeeding transformers contained 2 transposed convolutional layers with stride 2 and kernel size 3. Down and upsampling factors were set to  $M = 4$ . Channel compression lowered the number of channels from 512 to 256. Patch flattening was performed for a patch size of  $P = 1$ , corresponding to  $\mathbb{R}^{16 \times 16}$  patches in the original images. The transformer modules were based on the recent ViT architecture with 12 layers [56]. To minimize model complexity, transformer modules in ART blocks utilized tied weights and were only retained in the first and fifth blocks. Our cross-validation experiments indicated that this design yields optimal performance, with no noticeable gains from retention in other blocks. The dimensionality for latent representations in the transformer were set to  $N_d = 768$ . All models, including ResViT, employed the same PatchGAN discriminator. Code to replicate the ResViT model is publicly available at <https://github.com/icon-lab>.

### 4.4 Modeling Procedures

Here, all task-specific synthesis models were trained in an adversarial setup with adversarial and pixel-wise loss terms. In contrast, all unified synthesis models were trained with adversarial, pixel-wise, and additionally reconstruction loss terms. For fair comparisons, identical optimization procedures and weighting of the loss terms were employed for all competing methods. Learning rate schedules, number of epochs, and loss-term weighting were selected based on cross-validation. The selected set of parameters consistently yielded near-optimal performance in all methods. Model training was performed via the Adam optimizer [100] with  $\beta_1 = 0.5$ ,  $\beta_2 = 0.999$ . Model training was continued for 100 epochs, where the learning rate was 0.0002 for the first 50 epochs and linearly decayed to 0 in the remaining epochs. The only exceptions to this were TransUNet and ResViT that both utilize ViT modules which were pretrained for object classification tasks on the ImageNet database [101]; and ART blocks which were initially trained in the absence of ViT modules and later fine-tuned for 50 epochs. Relative weights for loss terms were  $\lambda_{adv} = 1$ ,  $\lambda_{pix} = 100$  for task-specific models, and  $\lambda_{adv} = 1$ ,  $\lambda_{rec} = 100$ ,  $\lambda_{pix} = 100$  for unified models.

### 4.5 Evaluation Metrics

We assessed the quality of synthesized images in terms of Peak Signal to Noise Ratio (PSNR), and Structural Similarity Index (SSIM) [102]. We calculated PSNR and SSIM between the ground truth and synthesized target images for the proposed model and competing methods in each task. Mean and standard deviations of model performances were reported across an independent test set, which did not overlap with the training and validation sets.

### 4.6 Experiments

**Multi-Contrast MRI Synthesis** Experiments were conducted on the IXI and BRATS datasets to demonstrate synthesis performance in multi-modal MRI. In the IXI dataset, one-to-one tasks of  $T_2 \rightarrow PD$ ;  $PD \rightarrow T_2$  and many-to-one tasks of  $T_1$ ,  $T_2 \rightarrow PD$ ;  $T_1$ ,  $PD \rightarrow T_2$ ;  $T_2$ ,  $PD \rightarrow T_1$  were considered. In the BRATS dataset, one-to-one tasks of  $T_2 \rightarrow FLAIR$ ;  $FLAIR \rightarrow T_2$ , many-to-one tasks of  $T_1$ ,  $T_2 \rightarrow FLAIR$ ;  $T_1$ ,  $FLAIR \rightarrow T_2$ ;  $T_2$ ,  $FLAIR \rightarrow T_1$  were considered.

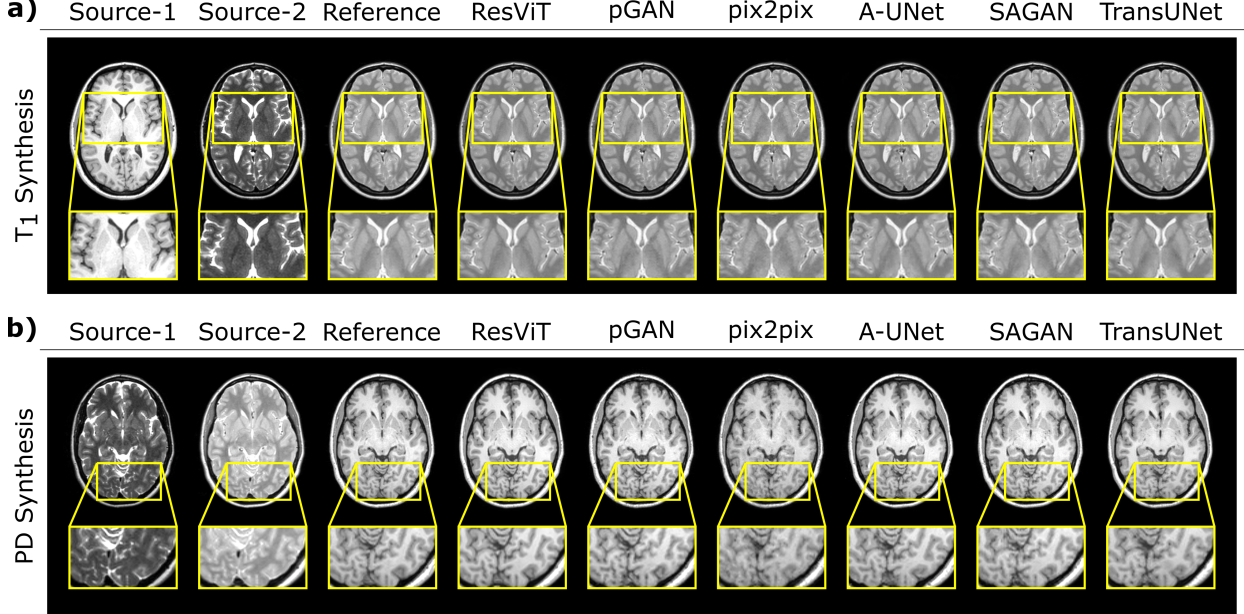


Figure 3: ResViT was demonstrated on the IXI dataset for two representative many-to-one synthesis tasks: a)  $T_1, T_2 \rightarrow PD$ , b)  $T_2, PD \rightarrow T_1$ . Synthesized images from all competing methods are shown along with the source images and the reference target image. ResViT improves synthesis performance in regions that are depicted sub-optimally in competing methods. Overall, ResViT generates images with lower artifact and noise levels and sharper tissue depiction.

In both datasets, task-specific ResViT models were compared against pGAN, pix2pix, A-UNet, SAGAN, and TransUNet. Meanwhile, unified ResViT models were demonstrated against pGAN<sub>uni</sub>, MM-GAN, and TransUNet<sub>uni</sub>.

**MRI to CT Synthesis** Experiments were performed on the MRI-CT dataset to demonstrate across-modality synthesis performance. A one-to-one synthesis task of deriving target CT images from source MR images was considered. The task-specific ResViT model was compared against pGAN, pix2pix, A-UNet, SAGAN, and TransUNet.

## 5 Results

### 5.1 Multi-Contrast MRI Synthesis

**Task-Specific Synthesis Models** We demonstrated the performance of ResViT in learning task-specific synthesis models for multi-contrast MRI. For this purpose, ResViT was compared against five different state-of-the-art baselines, including convolutional GANs (pGAN, pix2pix), attention GANs (A-UNet, SAGAN), and a hybrid CNN-transformer architecture (TransUNet). First, brain images of healthy subjects in the IXI dataset were considered. Three many-to-one tasks ( $T_1, T_2 \rightarrow PD$ ,  $T_1, PD \rightarrow T_2$ ,  $T_2, PD \rightarrow T_1$ ) and two one-to-one tasks ( $T_2 \rightarrow PD$ ,  $PD \rightarrow T_2$ ) were evaluated. PSNR and SSIM metrics for all methods are listed in Tables 1 and 2. ResViT achieves the highest performance in each individual many-to-one and one-to-one task. On average across all tasks, ResViT outperforms convolutional GANs by 1.62 dB PSNR and 0.85% SSIM, attention-based GANs by 1.40 dB PSNR and 1.45% SSIM, and TransUNet by 2.10 dB PSNR and 1.26% SSIM. Representative target images from all methods for  $T_1, T_2 \rightarrow PD$  and  $T_2, PD \rightarrow T_1$  are displayed in Figure 3 a,b, respectively. Compared to baselines, ResViT synthesizes target images with lower artifact levels and sharper tissue depiction.

We then demonstrated task-specific ResViT models on the BRATS dataset, which contains brain images of glioma patients. Three many-to-one tasks ( $T_1, T_2 \rightarrow FLAIR$ ,  $T_1, FLAIR \rightarrow T_2$ ,  $T_2, FLAIR \rightarrow T_1$ ) and two one-to-one tasks ( $T_2 \rightarrow FLAIR$ ,  $FLAIR \rightarrow T_2$ ) were evaluated. PSNR and SSIM metrics for many-to-one and one-to-one tasks are listed in Tables 3 and 4, respectively. Similar to the results on healthy subjects, ResViT achieves the highest performance in each individual many-to-one and one-to-one task performed on the BRATS dataset (except for SSIM in  $T_2 \rightarrow FLAIR$  where A-UNet and ResViT perform similarly). On average across tasks, ResViT outperforms convolutional GANs by 0.92 dB PSNR and 1.29% SSIM, attention-based GANs by 0.84 dB PSNR and 1.24% SSIM, and TransUNet by 0.94 dB PSNR and 1.10% SSIM. Note that the BRATS dataset contains pathology with large across-subject variability. As

	$T_1, T_2 \rightarrow PD$		$T_1, PD \rightarrow T_2$		$T_2, PD \rightarrow T_1$	
	PSNR	SSIM	PSNR	SSIM	PSNR	SSIM
ResViT	<b>33.92</b> <b><math>\pm 2.69</math></b>	<b>0.977</b> <b><math>\pm 0.008</math></b>	<b>35.71</b> <b><math>\pm 1.77</math></b>	<b>0.977</b> <b><math>\pm 0.008</math></b>	<b>29.58</b> <b><math>\pm 2.45</math></b>	<b>0.952</b> <b><math>\pm 0.025</math></b>
	32.91 $\pm 2.23$	0.966 $\pm 0.010$	33.95 $\pm 1.67$	0.965 $\pm 0.011$	28.71 $\pm 2.26$	0.941 $\pm 0.026$
pix2pix	32.25 $\pm 2.66$	0.974 $\pm 0.009$	33.62 $\pm 2.07$	0.973 $\pm 0.010$	28.35 $\pm 3.12$	0.949 $\pm 0.027$
A-UNet	32.24 $\pm 2.27$	0.963 $\pm 0.011$	32.43 $\pm 1.74$	0.959 $\pm 0.013$	28.95 $\pm 2.44$	0.916 $\pm 0.028$
SAGAN	32.50 $\pm 2.22$	0.964 $\pm 0.011$	33.71 $\pm 1.61$	0.965 $\pm 0.011$	28.62 $\pm 2.27$	0.942 $\pm 0.028$
TransUNet	32.53 $\pm 2.26$	0.968 $\pm 0.010$	32.49 $\pm 1.74$	0.960 $\pm 0.013$	28.21 $\pm 2.36$	0.941 $\pm 0.027$

Table 1: Performance of task-specific synthesis models in many-to-one tasks ( $T_1, T_2 \rightarrow PD$ ,  $T_1, PD \rightarrow T_2$ , and  $T_2, PD \rightarrow T_1$ ) in the IXI dataset. PSNR (dB) and SSIM (%) measurements are listed as mean $\pm$ std across test subjects. Boldface indicates the model with the top performance for a given task.

	ResViT	pGAN	pix2pix	A-UNet	SAGAN	TransUNet
PD	PSNR	<b>32.90</b> <b><math>\pm 2.56</math></b>	32.20 $\pm 2.19$	30.72 $\pm 2.42$	32.05 $\pm 2.44$	32.07 $\pm 2.26$
	SSIM	<b>0.972</b> <b><math>\pm 0.015</math></b>	0.963 $\pm 0.012$	0.956 $\pm 0.016$	0.960 $\pm 0.020$	0.963 $\pm 0.013$
$T_2 \rightarrow T_2$	PSNR	<b>34.24</b> <b><math>\pm 1.66</math></b>	33.05 $\pm 1.55$	30.74 $\pm 2.04$	33.32 $\pm 1.68$	32.96 $\pm 1.50$
	SSIM	<b>0.972</b> <b><math>\pm 0.008</math></b>	0.963 $\pm 0.012$	0.950 $\pm 0.016$	0.961 $\pm 0.015$	0.962 $\pm 0.012$
PD	PSNR	<b>30.90</b> <b><math>\pm 2.40</math></b>				
	SSIM	0.960 $\pm 0.014$				

Table 2: Performance of task-specific synthesis models in one-to-one tasks ( $T_2 \rightarrow PD$  and  $PD \rightarrow T_2$ ) in the IXI dataset. PSNR (dB) and SSIM (%) measurements are listed as mean $\pm$ std across test subjects. Boldface indicates the model with the top performance for a given task.

expected, attention-based GANs show some benefits in terms of relative performance against convolutional GANs, yet ResViT that explicitly models contextual relationships still outperforms attention GAN models. Representative target images from all methods for  $T_1, T_2 \rightarrow$  FLAIR and  $T_2, FLAIR \rightarrow T_1$  are displayed in Figure 4 a,b, respectively. Compared to baselines, ResViT synthesizes target images with lower artifact levels and sharper tissue depiction. Most critically, ResViT reliably captures brain lesions in patients in contrast to competing methods with inaccurate depictions, including TransUNet.

Superior depiction of pathology in ResViT signals the importance of aggregated transformer blocks in simultaneously maintaining local precision and contextual consistency in medical image synthesis. Although TransUNet also employs a transformer to capture context, it yields suboptimal synthesis quality in various tasks. This performance loss might be associated with two fundamental differences between the models. First, TransUNet forces CNN-based feature maps from its encoder through a transformer, while it uses skip connections to propagate only shallow convolutional features from earlier layers. ResViT instead continues encoding and propagating convolutional features across the information bottleneck, creating a much deeper and better-distilled feature representation. Importantly, residual skip connections within ART blocks are critical to ResViT’s performance, as we have observed in our validation studies. Second, the decoder in TransUNet performs bilinear upsampling to progressively increase the spatial resolution of synthesized images [47]. Several prior studies have suggested that bilinear interpolation might be suboptimal in suppressing high-frequency artifacts [103, 104]. In ResViT, we employ transposed convolutions within the upsampler modules in ART blocks and within the decoder to mitigate potential artifacts.

**Unified Synthesis Models** Experiments up to this point evaluated the performance of task-specific synthesis models, where each model was tested on the very task that it was trained to perform. While task-specific modeling can maximize performance, a separate model has to be built for each task, reducing practicality. Next, we demonstrated ResViT

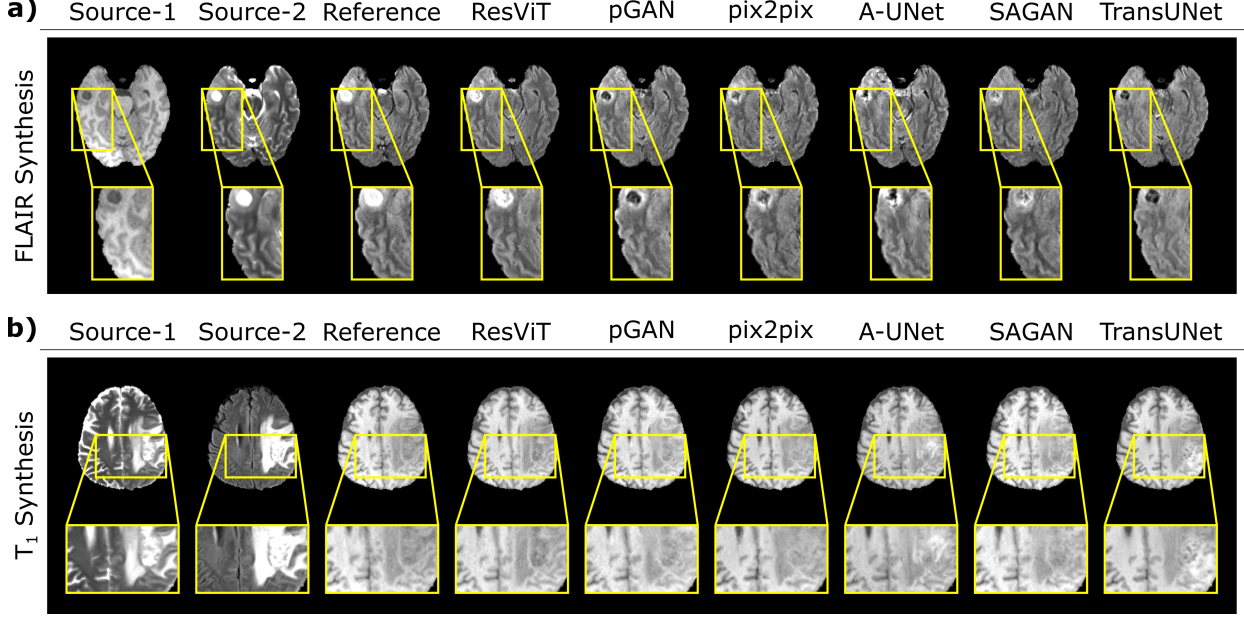


Figure 4: ResViT was demonstrated on the BRATS dataset for two representative many-to-one synthesis tasks: a)  $T_1, T_2 \rightarrow \text{FLAIR}$ , b)  $T_2, \text{FLAIR} \rightarrow T_1$ . Synthesized images from all competing methods are shown along with the source images and the reference image. ResViT improves synthesis performance, especially in pathological regions (e.g., tumors, lesions) in comparison to competing methods. Overall, ResViT images have better-delineated tissue boundaries and lower artifact/noise levels.

	$T_1, T_2 \rightarrow \text{FLAIR}$		$T_1, \text{FLAIR} \rightarrow T_2$		$T_2, \text{FLAIR} \rightarrow T_1$	
	PSNR	SSIM	PSNR	SSIM	PSNR	SSIM
ResViT	<b>25.80</b> $\pm 2.68$	<b>0.886</b> $\pm 0.030$	<b>26.90</b> $\pm 1.75$	<b>0.935</b> $\pm 0.020$	<b>26.20</b> $\pm 2.58$	<b>0.924</b> $\pm 0.021$
pGAN	24.89 $\pm 2.44$	0.867 $\pm 0.033$	26.51 $\pm 1.80$	0.922 $\pm 0.024$	25.72 $\pm 2.83$	0.918 $\pm 0.024$
pix2pix	24.31 $\pm 2.74$	0.862 $\pm 0.035$	26.12 $\pm 1.90$	0.920 $\pm 0.023$	25.80 $\pm 2.91$	0.918 $\pm 0.025$
A-UNet	24.36 $\pm 2.52$	0.857 $\pm 0.036$	26.48 $\pm 1.87$	0.924 $\pm 0.022$	25.67 $\pm 2.52$	0.918 $\pm 0.023$
SAGAN	24.62 $\pm 2.53$	0.869 $\pm 0.032$	26.41 $\pm 1.75$	0.919 $\pm 0.024$	25.91 $\pm 2.70$	0.918 $\pm 0.025$
TransUNet	24.34 $\pm 2.86$	0.872 $\pm 0.033$	26.51 $\pm 1.46$	0.920 $\pm 0.022$	25.76 $\pm 2.94$	0.921 $\pm 0.023$

Table 3: Performance of task-specific synthesis models in many-to-one tasks ( $T_1, T_2 \rightarrow \text{FLAIR}$ ,  $T_1, \text{FLAIR} \rightarrow T_2$ , and  $T_2, \text{FLAIR} \rightarrow T_1$ ) in the BRATS dataset. PSNR (dB) and SSIM (%) measurements are listed as mean $\pm$ std across test subjects. Boldface indicates the model with the top performance for a given task.

in learning unified synthesis models for multi-contrast MRI. The unified version of the proposed model, ResViT<sub>uni</sub>, was compared against three state-of-the-art baselines, including unified convolutional GANs (pGAN<sub>uni</sub>, MM-GAN), and a unified hybrid CNN-transformer architecture (TransUNet<sub>uni</sub>). Brain images from IXI and BRATS datasets were considered again. Performance of unified models were evaluated at test time on three many-to-one tasks in IXI ( $T_1, T_2 \rightarrow \text{PD}$ ,  $T_1, \text{PD} \rightarrow T_2$ ,  $T_2, \text{PD} \rightarrow T_1$ ) and in BRATS ( $T_1, T_2 \rightarrow \text{FLAIR}$ ,  $T_1, \text{FLAIR} \rightarrow T_2$ ,  $T_2, \text{FLAIR} \rightarrow T_1$ ). Corresponding performance metrics for IXI and BRATS are listed in Tables 5 and 6. Compared to baselines, ResViT<sub>uni</sub> maintains the highest performance in each synthesis task. In the IXI dataset, ResViT<sub>uni</sub> outperforms pGAN<sub>uni</sub> by 1.12 dB PSNR and 0.70% SSIM, MM-GAN by 2.37 dB PSNR and 1.80% SSIM, and TransUNet<sub>uni</sub> by 2.69 dB PSNR and 1.67% SSIM. Similarly, in the BRATS dataset, ResViT outperforms pGAN<sub>uni</sub> by 0.74 dB PSNR and 0.93% SSIM, MM-GAN by 0.77 dB PSNR and 0.90% SSIM, and TransUNet<sub>uni</sub> by 1.08 dB PSNR and 1.43% SSIM. Representative

	ResViT	pGAN	pix2pix	A-UNet	SAGAN	TransUNet	
FLAIR $\rightarrow$ T <sub>2</sub>	PSNR	<b>24.97</b> $\pm 2.58$	24.01 $\pm 2.85$	23.15 $\pm 2.58$	23.69 $\pm 3.34$	24.02 $\pm 3.03$	23.70 $\pm 3.22$
	SSIM	0.870 $\pm 0.034$	0.864 $\pm 0.035$	0.869 $\pm 0.034$	<b>0.873</b> $\pm 0.032$	0.860 $\pm 0.035$	0.864 $\pm 0.034$
	PSNR	<b>25.78</b> $\pm 1.56$	25.09 $\pm 2.56$	24.52 $\pm 2.38$	24.56 $\pm 1.57$	25.10 $\pm 1.39$	24.62 $\pm 1.37$
	SSIM	<b>0.908</b> $\pm 0.030$	0.894 $\pm 0.032$	0.883 $\pm 0.035$	0.891 $\pm 0.029$	0.893 $\pm 0.031$	0.891 $\pm 0.032$

Table 4: Performance of task-specific synthesis models in one-to-one tasks ( $T_2 \rightarrow$ FLAIR and FLAIR  $\rightarrow T_2$ ) in the BRATS dataset. PSNR (dB) and SSIM (%) measurements are listed as mean  $\pm$  std across test subjects. Boldface indicates the model with the top performance for a given task.

	$T_1, T_2 \rightarrow PD$		$T_1, PD \rightarrow T_2$		$T_2, PD \rightarrow T_1$	
	PSNR	SSIM	PSNR	SSIM	PSNR	SSIM
ResViT <sub>uni</sub>	<b>33.22</b> $\pm 2.46$	<b>0.971</b> $\pm 0.010$	<b>33.97</b> $\pm 1.62$	<b>0.968</b> $\pm 0.011$	<b>28.80</b> $\pm 2.42$	<b>0.946</b> $\pm 0.028$
pGAN <sub>uni</sub>	31.86 $\pm 2.35$	0.965 $\pm 0.012$	32.90 $\pm 1.51$	0.962 $\pm 0.012$	27.86 $\pm 2.21$	0.937 $\pm 0.031$
MM-GAN	30.73 $\pm 2.28$	0.955 $\pm 0.013$	30.91 $\pm 2.15$	0.951 $\pm 0.018$	27.23 $\pm 2.29$	0.925 $\pm 0.032$
TransUNet <sub>uni</sub>	30.30 $\pm 2.54$	0.956 $\pm 0.013$	30.77 $\pm 1.73$	0.949 $\pm 0.019$	26.86 $\pm 2.47$	0.930 $\pm 0.032$

Table 5: Performance of unified synthesis models in many-to-one tasks  $T_1, T_2 \rightarrow PD$ ,  $T_1, PD \rightarrow T_2$ , and  $T_2, PD \rightarrow T_1$  in the IXI dataset. PSNR (dB) and SSIM (%) measurements are listed as mean  $\pm$  std across test subjects. Boldface indicates the model with the top performance for a given task.

target images from all methods are displayed in Figure 5. Similar to the results for task-specific synthesis models, ResViT synthesizes target images with lower artifact levels and sharper tissue depiction than baselines in the unified setting. These results suggest that a unified ResViT model can be successfully built to consolidate models for varying source-target configurations.

## 5.2 Across-Modality Synthesis

Lastly, we demonstrated ResViT in learning across-modality synthesis models.  $T_2$ -weighted MRI and CT images in the pelvic MRI-CT dataset were considered. ResViT was compared against convolutional GANs (pGAN, pix2pix), attention-based GANs (A-UNet, SAGAN), and TransUNet. Synthesis of CT images given MRI images was evaluated.

	$T_1, T_2 \rightarrow$ FLAIR		$T_1, \text{FLAIR} \rightarrow T_2$		$T_2, \text{FLAIR} \rightarrow T_1$	
	PSNR	SSIM	PSNR	SSIM	PSNR	SSIM
ResViT <sub>uni</sub>	<b>25.32</b> $\pm 2.44$	<b>0.876</b> $\pm 0.032$	<b>26.81</b> $\pm 1.68$	<b>0.921</b> $\pm 0.023$	<b>26.24</b> $\pm 2.58$	<b>0.922</b> $\pm 0.023$
pGAN <sub>uni</sub>	24.46 $\pm 2.27$	0.865 $\pm 0.034$	26.23 $\pm 1.70$	0.914 $\pm 0.026$	25.46 $\pm 2.47$	0.912 $\pm 0.025$
MM-GAN	24.20 $\pm 2.81$	0.861 $\pm 0.037$	26.10 $\pm 1.88$	0.915 $\pm 0.026$	25.75 $\pm 2.69$	0.916 $\pm 0.025$
TransUNet <sub>uni</sub>	24.11 $\pm 2.66$	0.863 $\pm 0.033$	26.05 $\pm 1.92$	0.912 $\pm 0.023$	24.96 $\pm 2.47$	0.901 $\pm 0.028$

Table 6: Performance of unified synthesis models in many-to-one tasks ( $T_1, T_2 \rightarrow$ FLAIR,  $T_1, \text{FLAIR} \rightarrow T_2$ , and  $T_2, \text{FLAIR} \rightarrow T_1$ ) in the BRATS dataset. PSNR (dB) and SSIM (%) measurements are listed as mean  $\pm$  std across test subjects. Boldface indicates the model with the top performance for a given task.

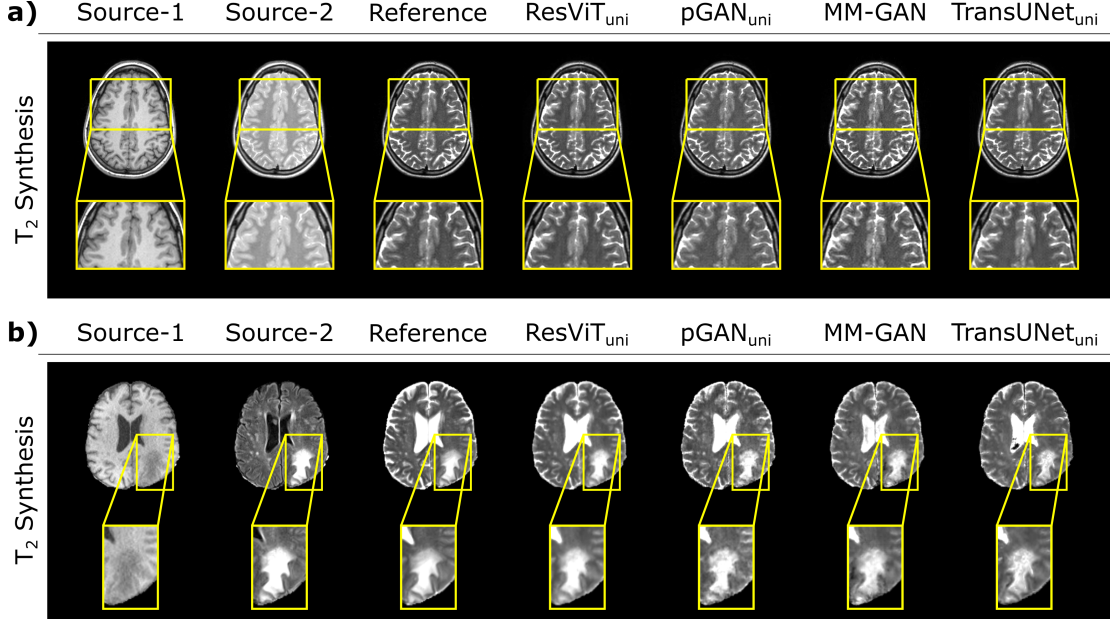


Figure 5: ResViT<sub>uni</sub> was demonstrated against other unified models on brain MRI datasets for two representative tasks: a) T<sub>1</sub>, PD → T<sub>2</sub> in IXI, b) T<sub>1</sub>, T<sub>2</sub> → FLAIR in BRATS. Synthesized images from all competing methods are shown along with the source images and the reference target image. ResViT<sub>uni</sub> improves synthesis performance especially in pathological regions (tumors, lesions) in comparison to competing methods. Overall, ResViT<sub>uni</sub> generates images with lower artifact and noise levels and more accurate tissue depiction for tasks in both datasets.

	ResViT	pGAN	pix2pix	A-UNet	SAGAN	TransUNet
MRI → CT	<b>28.45</b> ±2.32	26.80 ±2.04	26.53 ±1.96	27.80 ±3.29	27.61 ±2.01	27.76 ±2.29
	<b>0.931</b> ±0.018	0.905 ±0.020	0.898 ±0.023	0.913 ±0.054	0.910 ±0.020	0.914 ±0.020

Table 7: Performance for the across-modality synthesis task (T<sub>2</sub>-weighted MRI → CT) in the pelvic MRI-CT dataset. PSNR (dB) and SSIM (%) measurements are listed as mean±std across test subjects. Boldface indicates the model with the top performance for a given task.

PSNR and SSIM metrics for all methods are listed in Table 7. ResViT achieves the highest performance in this task. ResViT outperforms convolutional GANs by 1.79 dB PSNR and 2.95% SSIM, attention GANs by 0.75 dB PSNR and 1.95% SSIM, and TransUNet by 0.69 dB PSNR and 1.7% SSIM. Representative target images from all methods are displayed in Figure 6. Compared to baselines, ResViT synthesizes target images with lower artifacts and more accurate tissue depiction. Unlike in multi-contrast MRI, attention GANs and TransUNet perform better than convolutional GANs in this particular task. That said, ResViT still maintains further elevated synthesis performance compared to all baselines, particularly near relevant bone structures in CT images. This finding suggests that global representation of context is relatively more critical against the local representation of structural details in MRI-CT synthesis. With the help of its residual transformer blocks, ResViT offers reliable performance with accurate tissue depiction in this across-modality task.

## 6 Discussion

In this study, we proposed a novel generative adversarial approach for image translation between separate modalities. Traditional GANs for image synthesis employ convolutional operators that have limited ability to capture long-range relationships among distant regions [47, 48]. The proposed approach aggregates convolutional and transformer branches within a residual information bottleneck to preserve both local precision and contextual sensitivity. To our knowledge, this is the first adversarial model for medical image synthesis to leverage aggregated residual transformer (ART) blocks. We further introduced a weight-sharing strategy among ART blocks to lower model complexity. Finally, a unification

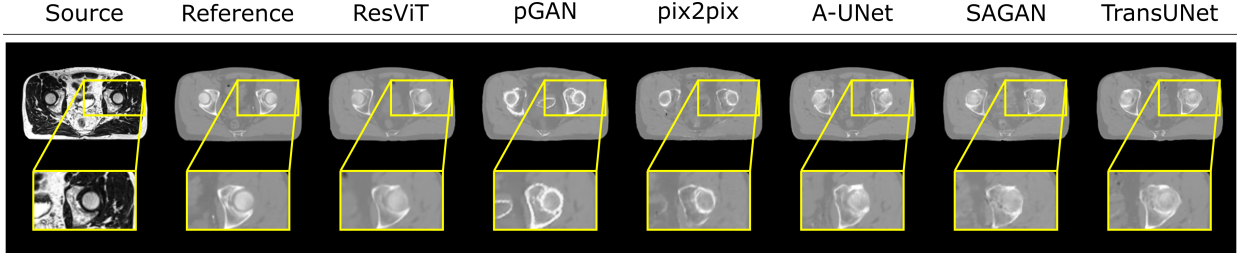


Figure 6: ResViT was demonstrated on the pelvic MRI-CT dataset for the T<sub>2</sub>-weighted MRI → CT task. Synthesized images from all competing methods are shown along with the source and reference images. ResViT enhances synthesis of relevant morphology in the CT domain as evidenced by the elevated accuracy near bone structures.

strategy was implemented to learn an aggregate model that copes with numerous source-target configurations without training separate models.

We comprehensively demonstrated ResViT for missing sequence synthesis tasks in multi-contrast MRI and missing modality synthesis in multi-modal MRI-CT imaging. Comparisons were provided against state-of-the-art GAN models for image synthesis, including CNN-based adversarial models with UNet and ResNet backbones and a recent transformer architecture with UNet backbone (TransUNet). ResViT outperforms all competing methods in both one-to-one and many-to-one synthesis tasks. Our results clearly demonstrate the efficiency of the residual transformer blocks in ResViT in maintaining contextual and local representations.

Trained with image-average loss terms, CNNs have difficulty in generalizing to atypical anatomy that substantially varies across subjects [25, 32]. To improve generalization performance, recent studies have proposed self-attention mechanisms in GAN models over spatial or channel dimensions in various medical imaging tasks [53, 58]. Specifically, attention maps are used for multiplicative modulation of CNN-derived feature maps. This attentional modulation encourages the network to focus on critical image regions with relatively limited task performance. While attention maps can be distributed across broad image regions, they mainly capture implicit contextual information via modification of local CNN features. In contrast, the proposed architecture uses dedicated transformer blocks to explicitly model long-range spatial interactions in medical images.

Several lines of methodological development can help further improve ResViT’s performance. In this study, we considered synthesis tasks in which source and target modalities were registered prior to model training, and they were collected from the same set of subjects. In cases where registration accuracy is limited due to a substantial resolution mismatch between source-target modalities, a spatial transformer block can be incorporated into the network architecture to perform multi-modal registration. Furthermore, a cycle-consistency loss [46] can be incorporated in the optimization objective to allow the use of unregistered images. This latter strategy would also permit training of ResViT models on unpaired datasets [76, 77]. Finally, data requirements for model training can be further alleviated by adopting semi-supervised strategies that allow mixing of paired and unpaired training data [75], or that would enable training of synthesis models directly from undersampled acquisitions [43].

Here vision transformers included in TransUNet [47] and ResViT architectures were fine-tuned starting with versions pretrained on a large array of natural images from ImageNet [105]. This practice follows recent studies on NLP and computer vision that report suboptimal performance in transformers trained from scratch on relatively modest-sized datasets [47, 56]. This likely stems from the poorly conditioned optimization landscape of transformer models under gradient-descent algorithms. Recent optimizers sculpted specifically for transformers might potentially allow from-scratch training of medical image synthesis models without performance loss [106]. A recent alternative to transformer models based on self-attention mechanisms is attention-free architectures based on feedforward models such as MLP-mixers or AFT [107, 108], suggested to offer on par performance to transformers on generic computer vision tasks. It remains important for future work to examine whether attention-free models offer any benefits over transformer models in medical imaging tasks.

## 7 Conclusion

Here we introduced a novel synthesis approach for multi-modal imaging based on a conditional deep adversarial network. In an information bottleneck, the proposed ResViT model aggregates convolutional operators and vision transformers via residual blocks and thereby improves capture of contextual relations while maintaining localization power. The proposed model was comprehensively demonstrated for one-to-one and many-to-one tasks. Furthermore, a

unified implementation was introduced that prevents the need to rebuild models for varying source-target configurations. ResViT achieves superior synthesis quality to state-of-the-art approaches in multi-contrast brain MRI and multi-modal pelvic MRI-CT datasets. Therefore, it is a powerful candidate for medical image synthesis in clinical applications.

## References

- [1] B. J. Pichler, M. S. Judenhofer, and C. Pfannenberg, *Multimodal Imaging Approaches: PET/CT and PET/MRI*, pp. 109–132. Berlin, Heidelberg: Springer Berlin Heidelberg, 2008.
- [2] B. Moraal, S. Roosendaal, P. Pouwels, H. Vrenken, R. Schijndel, D. Meier, C. Guttmann, J. Geurts, and F. Barkhof, “Multi-contrast, isotropic, single-slab 3d MR imaging in multiple sclerosis,” *European radiology*, vol. 18, pp. 2311–20, 06 2008.
- [3] B. Thukral, “Problems and preferences in pediatric imaging,” *Indian Journal of Radiology and Imaging*, vol. 25, pp. 359–364, 2015.
- [4] K. Krupa and M. Bekiesińska-Figatowska, “Artifacts in magnetic resonance imaging,” *Polish Journal of Radiology / Polish Medical Society of Radiology*, vol. 80, pp. 93–106, 2015.
- [5] J. E. Iglesias, E. Konukoglu, D. Zikic, B. Glocker, K. Van Leemput, and B. Fischl, “Is synthesizing MRI contrast useful for inter-modality analysis?,” in *Medical Image Computing and Computer-Assisted Intervention – MICCAI*, pp. 631–638, Springer Berlin Heidelberg, 2013.
- [6] Y. Huo, Z. Xu, S. Bao, A. Assad, R. G. Abramson, and B. A. Landman, “Adversarial synthesis learning enables segmentation without target modality ground truth,” in *2018 IEEE 15th International Symposium on Biomedical Imaging (ISBI)*, pp. 1217–1220, 2018.
- [7] S. Farsiu, D. Robinson, M. Elad, and P. Milanfar, “Advances and challenges in super-resolution,” *International Journal of Imaging Systems and Technology*, vol. 14, 01 2004.
- [8] D. H. Ye, D. Zikic, B. Glocker, A. Criminisi, and E. Konukoglu, “Modality propagation: Coherent synthesis of subject-specific scans with data-driven regularization,” in *Medical Image Computing and Computer-Assisted Intervention – MICCAI 2013* (K. Mori, I. Sakuma, Y. Sato, C. Barillot, and N. Navab, eds.), (Berlin, Heidelberg), pp. 606–613, Springer Berlin Heidelberg, 2013.
- [9] C. Catana, A. van der Kouwe, T. Benner, C. J. Michel, M. Hamm, M. Fenchel, B. Fischl, B. Rosen, M. Schmand, and A. G. Sorensen, “Toward implementing an MRI-based PET attenuation-correction method for neurologic studies on the MR-PET brain prototype,” *Journal of Nuclear Medicine*, vol. 51, no. 9, pp. 1431–1438, 2010.
- [10] J. Lee, A. Carass, A. Jog, C. Zhao, and J. Prince, “Multi-atlas-based CT synthesis from conventional MRI with patch-based refinement for MRI-based radiotherapy planning,” vol. 10133, p. 101331I, 02 2017.
- [11] S. Roy, A. Jog, A. Carass, and J. L. Prince, “Atlas based intensity transformation of brain MR images,” in *Multimodal Brain Image Analysis* (L. Shen, T. Liu, P.-T. Yap, H. Huang, D. Shen, and C.-F. Westin, eds.), (Cham), pp. 51–62, Springer International Publishing, 2013.
- [12] Y. Huang, L. Shao, and A. F. Frangi, “Simultaneous super-resolution and cross-modality synthesis of 3d medical images using weakly-supervised joint convolutional sparse coding,” *2017 IEEE Conference on Computer Vision and Pattern Recognition (CVPR)*, pp. 5787–5796, 2017.
- [13] Y. Huang, L. Shao, and A. F. Frangi, “Cross-modality image synthesis via weakly coupled and geometry co-regularized joint dictionary learning,” *IEEE Transactions on Medical Imaging*, vol. 37, no. 3, pp. 815–827, 2018.
- [14] C. Zhao, A. Carass, J. Lee, Y. He, and J. L. Prince, “Whole brain segmentation and labeling from CT using synthetic MR images,” in *Machine Learning in Medical Imaging* (Q. Wang, Y. Shi, H.-I. Suk, and K. Suzuki, eds.), (Cham), pp. 291–298, Springer International Publishing, 2017.
- [15] A. Jog, A. Carass, S. Roy, D. L. Pham, and J. L. Prince, “Random forest regression for magnetic resonance image synthesis,” *Medical Image Analysis*, vol. 35, pp. 475–488, 2017.
- [16] H. Van Nguyen, K. Zhou, and R. Vemulapalli, “Cross-domain synthesis of medical images using efficient location-sensitive deep network,” in *Medical Image Computing and Computer-Assisted Intervention – MICCAI 2015* (N. Navab, J. Hornegger, W. M. Wells, and A. Frangi, eds.), (Cham), pp. 677–684, Springer International Publishing, 2015.
- [17] R. Vemulapalli, H. Van Nguyen, and S. K. Zhou, “Unsupervised cross-modal synthesis of subject-specific scans,” in *2015 IEEE International Conference on Computer Vision (ICCV)*, pp. 630–638, 2015.

[18] Y. Wu, W. Yang, L. Lu, Z. Lu, L. Zhong, M. Huang, Y. Feng, Q. Feng, and W. Chen, “Prediction of CT substitutes from MR images based on local diffeomorphic mapping for brain PET attenuation correction,” *Journal of Nuclear Medicine*, vol. 57, no. 10, pp. 1635–1641, 2016.

[19] D. C. Alexander, D. Zikic, J. Zhang, H. Zhang, and A. Criminisi, “Image quality transfer via random forest regression: Applications in diffusion MRI,” in *Medical Image Computing and Computer-Assisted Intervention – MICCAI 2014* (P. Golland, N. Hata, C. Barillot, J. Hornegger, and R. Howe, eds.), (Cham), pp. 225–232, Springer International Publishing, 2014.

[20] T. Huynh, Y. Gao, J. Kang, L. Wang, P. Zhang, J. Lian, and D. Shen, “Estimating CT image from MRI data using structured random forest and auto-context model,” *IEEE transactions on medical imaging*, vol. 35, 07 2015.

[21] P. Coupe, J. V. Manjón, M. Chamberland, M. Descoteaux, and B. Hiba, “Collaborative patch-based super-resolution for diffusion-weighted images,” *NeuroImage*, vol. 83, pp. 245–261, 2013.

[22] A. Chartsias, T. Joyce, M. V. Giuffrida, and S. A. Tsaftaris, “Multimodal MR synthesis via modality-invariant latent representation,” *IEEE Transactions on Medical Imaging*, vol. 37, no. 3, pp. 803–814, 2018.

[23] V. Sevetlidis, V. Giuffrida, and S. Tsaftaris, “Whole image synthesis using a deep encoder-decoder network,” pp. 127–137, 10 2016.

[24] T. Joyce, A. Chartsias, and S. A. Tsaftaris, “Robust multi-modal MR image synthesis,” in *Medical Image Computing and Computer Assisted Intervention MICCAI 2017* (M. Descoteaux, L. Maier-Hein, A. Franz, P. Jannin, D. L. Collins, and S. Duchesne, eds.), (Cham), pp. 347–355, Springer International Publishing, 2017.

[25] S. U. Dar, M. Yurt, L. Karacan, A. Erdem, E. Erdem, and T. Çukur, “Image synthesis in multi-contrast MRI with conditional generative adversarial networks,” *IEEE Transactions on Medical Imaging*, vol. 38, no. 10, pp. 2375–2388, 2019.

[26] M. Yurt, S. U. Dar, A. Erdem, E. Erdem, K. K. Oguz, and T. Çukur, “mustGAN: multi-stream generative adversarial networks for MR image synthesis,” *Medical Image Analysis*, vol. 70, p. 101944, 2021.

[27] D. Lee, J. Kim, W.-J. Moon, and J. C. Ye, “CollaGAN: Collaborative GAN for missing image data imputation,” in *Proceedings of the IEEE/CVF Conference on Computer Vision and Pattern Recognition (CVPR)*, June 2019.

[28] A. Sharma and G. Hamarneh, “Missing MRI pulse sequence synthesis using multi-modal generative adversarial network,” *IEEE Transactions on Medical Imaging*, vol. 39, pp. 1170–1183, 2020.

[29] C. Bowles, C. Qin, C. Ledig, R. Guerrero, R. Gunn, A. Hammers, E. Sakka, D. Dickie, M. Hernández, N. Royle, J. Wardlaw, H. Rhodius-Meester, B. Tijms, A. Lemstra, W. Flier, F. Barkhof, P. Scheltens, and D. Rueckert, “Pseudo-healthy image synthesis for white matter lesion segmentation,” pp. 87–96, 10 2016.

[30] N. Cordier, H. Delingette, M. Le, and N. Ayache, “Extended modality propagation: Image synthesis of pathological cases,” *IEEE transactions on medical imaging*, vol. 35, pp. 2598–2608, 07 2016.

[31] W. Wei, E. Poirion, B. Bodini, S. Durrleman, O. Colliot, B. Stankoff, and N. Ayache, “Fluid-attenuated inversion recovery MRI synthesis from multisequence MRI using three-dimensional fully convolutional networks for multiple sclerosis,” *Journal of Medical Imaging*, vol. 6, p. 1, 02 2019.

[32] P. Isola, J.-Y. Zhu, T. Zhou, and A. A. Efros, “Image-to-image translation with conditional adversarial networks,” *CVPR*, 2017.

[33] I. Goodfellow, J. Pouget-Abadie, M. Mirza, B. Xu, D. Warde-Farley, S. Ozair, A. Courville, and Y. Bengio, “Generative adversarial networks,” *Advances in Neural Information Processing Systems*, vol. 3, 06 2014.

[34] K. Armanious, C. Jiang, M. Fischer, T. Küstner, T. Hepp, K. Nikolaou, S. Gatidis, and B. Yang, “MedGAN: Medical image translation using GANs,” *Computerized Medical Imaging and Graphics*, vol. 79, p. 101684, 11 2019.

[35] A. Beers, J. Brown, K. Chang, J. Campbell, S. Ostmo, M. Chiang, and J. Kalpathy-Cramer, “High-resolution medical image synthesis using progressively grown generative adversarial networks,” 05 2018.

[36] H. Lan, A. Toga, and F. Sepehrband, “Sc-GAN: 3d self-attention conditional GAN with spectral normalization for multi-modal neuroimaging synthesis,” *bioRxiv*, 2020.

[37] H. Li, J. C. Paetzold, A. Sekuboyina, F. Kofler, J. Zhang, J. S. Kirschke, B. Wiestler, and B. Menze, “Diamondgan: Unified multi-modal generative adversarial networks for MRI sequences synthesis,” in *Medical Image Computing and Computer Assisted Intervention – MICCAI 2019* (D. Shen, T. Liu, T. M. Peters, L. H. Staib, C. Essert, S. Zhou, P.-T. Yap, and A. Khan, eds.), (Cham), pp. 795–803, Springer International Publishing, 2019.

[38] M. Yurt, M. Özbeý, S. U. H. Dar, B. Tinaz, K. K. Oğuz, and T. Çukur, “Progressively volumetrized deep generative models for data-efficient contextual learning of MR image recovery,” 2020.

[39] G. Wang, E. Gong, S. Banerjee, D. Martin, E. Tong, J. Choi, H. Chen, M. Wintermark, J. M. Pauly, and G. Zaharchuk, “Synthesize high-quality multi-contrast magnetic resonance imaging from multi-echo acquisition using multi-task deep generative model,” *IEEE Transactions on Medical Imaging*, vol. 39, no. 10, pp. 3089–3099, 2020.

[40] H. Yang, X. Lu, S.-H. Wang, Z. Lu, J. Yao, Y. Jiang, and P. Qian, “Synthesizing multi-contrast MR images via novel 3d conditional variational auto-encoding GAN,” *Mobile Networks and Applications*, vol. 26, pp. 1–10, 02 2021.

[41] B. Yu, L. Zhou, L. Wang, J. Fripp, and P. Bourgeat, “3d cGAN based cross-modality MR image synthesis for brain tumor segmentation,” *2018 IEEE 15th International Symposium on Biomedical Imaging (ISBI 2018)*, pp. 626–630, 2018.

[42] B. Yu, L. Zhou, L. Wang, Y. Shi, J. Fripp, and P. Bourgeat, “Ea-GANs: Edge-aware generative adversarial networks for cross-modality MR image synthesis,” *IEEE Transactions on Medical Imaging*, vol. 38, no. 7, pp. 1750–1762, 2019.

[43] M. Yurt, S. U. H. Dar, M. Özbey, B. Tınaz, K. K. Oğuz, and T. Çukur, “Semi-supervised learning of mutually accelerated MRI synthesis without fully-sampled ground truths,” 2021.

[44] T. Zhou, H. Fu, G. Chen, J. Shen, and L. Shao, “Hi-net: Hybrid-fusion network for multi-modal MR image synthesis,” *IEEE Transactions on Medical Imaging*, vol. 39, no. 9, pp. 2772–2781, 2020.

[45] D. Nie, R. Trullo, J. Lian, L. Wang, C. Petitjean, S. Ruan, and Q. Wang, “Medical image synthesis with deep convolutional adversarial networks,” *IEEE Transactions on Biomedical Engineering*, vol. PP, pp. 1–1, 03 2018.

[46] J.-Y. Zhu, T. Park, P. Isola, and A. A. Efros, “Unpaired image-to-image translation using cycle-consistent adversarial networks,” *2017 IEEE International Conference on Computer Vision (ICCV)*, pp. 2242–2251, 2017.

[47] J. Chen, Y. Lu, Q. Yu, X. Luo, E. Adeli, Y. Wang, L. Lu, A. L. Yuille, and Y. Zhou, “Transunet: Transformers make strong encoders for medical image segmentation,” 2021.

[48] N. Kodali, J. Hays, J. Abernethy, and Z. Kira, “On convergence and stability of GANs,” *arXiv: Artificial Intelligence*, 2018.

[49] H. Emami, M. Dong, and C. K. Glide-Hurst, “Attention-guided generative adversarial network to address atypical anatomy in modality transfer,” 2021.

[50] J. Schlemper, O. Oktay, M. Schaap, M. Heinrich, B. Kainz, B. Glocker, and D. Rueckert, “Attention gated networks: Learning to leverage salient regions in medical images,” *Medical image analysis*, vol. 53, pp. 197 – 207, 2019.

[51] X. Wang, R. Girshick, A. Gupta, and K. He, “Non-local neural networks,” in *2018 IEEE/CVF Conference on Computer Vision and Pattern Recognition*, pp. 7794–7803, 2018.

[52] W. Wei, E. Poirion, B. Bodini, M. Tonietto, S. Durrleman, O. Colliot, B. Stankoff, and N. Ayache, “Predicting PET-derived myelin content from multisequence MRI for individual longitudinal analysis in multiple sclerosis,” *NeuroImage*, vol. 223, p. 117308, 2020.

[53] H. Zhang, I. Goodfellow, D. Metaxas, and A. Odena, “Self-attention generative adversarial networks,” in *Proceedings of the 36th International Conference on Machine Learning* (K. Chaudhuri and R. Salakhutdinov, eds.), vol. 97 of *Proceedings of Machine Learning Research*, pp. 7354–7363, PMLR, 09–15 Jun 2019.

[54] A. Vaswani, N. M. Shazeer, N. Parmar, J. Uszkoreit, L. Jones, A. N. Gomez, L. Kaiser, and I. Polosukhin, “Attention is all you need,” *ArXiv*, vol. abs/1706.03762, 2017.

[55] J. Devlin, M.-W. Chang, K. Lee, and K. Toutanova, “Bert: Pre-training of deep bidirectional transformers for language understanding,” in *NAACL-HLT*, 2019.

[56] A. Dosovitskiy, L. Beyer, A. Kolesnikov, D. Weissenborn, X. Zhai, T. Unterthiner, M. Dehghani, M. Minderer, G. Heigold, S. Gelly, J. Uszkoreit, and N. Houlsby, “An image is worth 16x16 words: Transformers for image recognition at scale,” 2021.

[57] K. He, X. Zhang, S. Ren, and J. Sun, “Deep residual learning for image recognition,” in *2016 IEEE Conference on Computer Vision and Pattern Recognition (CVPR)*, pp. 770–778, 2016.

[58] O. Oktay, J. Schlemper, L. L. Folgoc, M. J. Lee, M. Heinrich, K. Misawa, K. Mori, S. G. McDonagh, N. Hammerla, B. Kainz, B. Glocker, and D. Rueckert, “Attention u-net: Learning where to look for the pancreas,” *ArXiv*, vol. abs/1804.03999, 2018.

[59] X. Yi, E. Walia, and P. Babyn, “Generative adversarial network in medical imaging: A review,” *Medical Image Analysis*, vol. 58, p. 101552, 2019.

[60] G. Litjens, T. Kooi, B. E. Bejnordi, A. A. A. Setio, F. Ciompi, M. Ghafoorian, J. A. van der Laak, B. van Ginneken, and C. I. Sánchez, “A survey on deep learning in medical image analysis,” *Medical Image Analysis*, vol. 42, pp. 60–88, 2017.

[61] R. Li, W. Zhang, H.-I. Suk, L. Wang, J. Li, D. Shen, and S. Ji, “Deep learning based imaging data completion for improved brain disease diagnosis,” in *Medical Image Computing and Computer-Assisted Intervention – MICCAI 2014* (P. Golland, N. Hata, C. Barillot, J. Hornegger, and R. Howe, eds.), (Cham), pp. 305–312, Springer International Publishing, 2014.

[62] A. Torrado-Carvajal, J. L. Herraiz, E. Alcain, A. S. Montemayor, L. Garcia-Cañamaque, J. A. Hernandez-Tamames, Y. Rozenholc, and N. Malpica, “Fast patch-based pseudo-CT synthesis from t1-weighted MR images for PET/MR attenuation correction in brain studies,” *Journal of Nuclear Medicine*, vol. 57, no. 1, pp. 136–143, 2016.

[63] K. Bahrami, F. Shi, I. Rekik, and D. Shen, “Convolutional neural network for reconstruction of 7t-like images from 3t MRI using appearance and anatomical features,” in *Deep Learning and Data Labeling for Medical Applications* (G. Carneiro, D. Mateus, L. Peter, A. Bradley, J. M. R. S. Tavares, V. Belagiannis, J. P. Papa, J. C. Nascimento, M. Loog, Z. Lu, J. S. Cardoso, and J. Cornebise, eds.), (Cham), pp. 39–47, Springer International Publishing, 2016.

[64] K. Bahrami, F. Shi, X. Zong, H. W. Shin, H. An, and D. Shen, “Reconstruction of 7t-like images from 3t MRI,” *IEEE Transactions on Medical Imaging*, vol. 35, no. 9, pp. 2085–2097, 2016.

[65] Y. Zhang, P.-T. Yap, L. Qu, J.-Z. Cheng, and D. Shen, “Dual-domain convolutional neural networks for improving structural information in 3t MRI,” *Magnetic Resonance Imaging*, vol. 64, pp. 90–100, 2019. Artificial Intelligence in MRI.

[66] X. Han, “MR-based synthetic CT generation using a deep convolutional neural network method,” *Medical Physics*, vol. 44, no. 4, pp. 1408–1419, 2017.

[67] D. Nie, X. Cao, Y. Gao, L. Wang, and D. Shen, “Estimating CT image from MRI data using 3d fully convolutional networks,” in *Deep Learning and Data Labeling for Medical Applications* (G. Carneiro, D. Mateus, L. Peter, A. Bradley, J. M. R. S. Tavares, V. Belagiannis, J. P. Papa, J. C. Nascimento, M. Loog, Z. Lu, J. S. Cardoso, and J. Cornebise, eds.), (Cham), pp. 170–178, Springer International Publishing, 2016.

[68] H. Arabi, G. Zeng, G. Zheng, and H. Zaidi, “Novel deep learning-based CT synthesis algorithm for MRI-guided PET attenuation correction in brain PET/MR imaging,” in *2018 IEEE Nuclear Science Symposium and Medical Imaging Conference Proceedings (NSS/MIC)*, pp. 1–3, 2018.

[69] K. Klaser, T. Varsavsky, P. Markiewicz, T. Vercauteran, D. Atkinson, K. Thielemans, B. Hutton, M. J. Cardoso, and S. Ourselin, “Improved MR to CT synthesis for PET/MR attenuation correction using imitation learning,” in *Simulation and Synthesis in Medical Imaging* (N. Burgos, A. Gooya, and D. Svoboda, eds.), (Cham), pp. 13–21, Springer International Publishing, 2019.

[70] M. Mirza and S. Osindero, “Conditional generative adversarial nets,” 2014.

[71] V. Sandfort, K. Yan, P. Pickhardt, and R. Summers, “Data augmentation using generative adversarial networks (cycleGAN) to improve generalizability in CT segmentation tasks,” *Scientific Reports*, vol. 9, 11 2019.

[72] M. Frid-Adar, I. Diamant, E. Klang, M. Amitai, J. Goldberger, and H. Greenspan, “GAN-based synthetic medical image augmentation for increased cnn performance in liver lesion classification,” *Neurocomputing*, vol. 321, pp. 321–331, 2018.

[73] A. Ben-Cohen, E. Klang, S. Raskin, S. Soffer, S. Ben-Haim, E. Konen, M. Amitai, and H. Greenspan, “Cross-modality synthesis from CT to PET using FCN and GAN networks for improved automated lesion detection,” *Engineering Applications of Artificial Intelligence*, vol. 78, 02 2018.

[74] G. Santini, C. Fourcade, N. Moreau, C. Rousseau, L. Ferrer, M. Lacombe, V. Fleury, M. Campone, P. Jezequel, and M. Rubeaux, “Unpaired PET/CT image synthesis of liver region using CycleGAN,” in *16th International Symposium on Medical Information Processing and Analysis* (J. Brieva, N. Lepore, M. G. Linguraru, and E. R. C. M.D., eds.), vol. 11583, pp. 247 – 257, International Society for Optics and Photonics, SPIE, 2020.

[75] C.-B. Jin, H. Kim, M. Liu, W. Jung, S. Joo, E. Park, Y. S. Ahn, I. H. Han, J. I. Lee, and X. Cui, “Deep CT to MR synthesis using paired and unpaired data,” *Sensors*, vol. 19, no. 10, 2019.

[76] Y. Ge, D. Wei, Z. Xue, Q. Wang, X. Zhou, Y. Zhan, and S. Liao, “Unpaired MR to CT synthesis with explicit structural constrained adversarial learning,” in *2019 IEEE 16th International Symposium on Biomedical Imaging (ISBI 2019)*, pp. 1096–1099, 2019.

[77] J. Wolterink, A. M. Dinkla, M. Savenije, P. Seevinck, C. Berg, and I. Igum, “Deep MR to CT synthesis using unpaired data,” in *SASHIMI@MICCAI*, 2017.

[78] X. Dong, T. Wang, Y. Lei, K. Higgins, T. Liu, W. Curran, H. Mao, J. Nye, and X. Yang, “Synthetic CT generation from non-attenuation corrected PET images for whole-body PET imaging,” *Physics in Medicine and Biology*, vol. 64, 10 2019.

[79] H. Yang, J. Sun, A. Carass, C. Zhao, J. Lee, Z. Xu, and J. Prince, “Unpaired brain MR-to-CT synthesis using a structure-constrained cycleGAN,” 2018.

[80] Y. Hiasa, Y. Otake, M. Takao, T. Matsuoka, K. Takashima, J. Prince, N. Sugano, and Y. Sato, “Cross-modality image synthesis from unpaired data using cycleGAN: Effects of gradient consistency loss and training data size,” 03 2018.

[81] A. Chartsias, T. Joyce, R. Dharmakumar, and S. A. Tsaftaris, “Adversarial image synthesis for unpaired multi-modal cardiac data,” in *Simulation and Synthesis in Medical Imaging* (S. A. Tsaftaris, A. Gooya, A. F. Frangi, and J. L. Prince, eds.), (Cham), pp. 3–13, Springer International Publishing, 2017.

[82] H. Do, P. Bourdon, D. Helbert, M. Naudin, and R. Guillemin, “7t MRI super-resolution with generative adversarial network,” in *IST Electronic Imaging 2021 Symposium*, 2021.

[83] L. Xiang, Y. Li, W. Lin, Q. Wang, and D. Shen, “Unpaired deep cross-modality synthesis with fast training,” in *Deep Learning in Medical Image Analysis and Multimodal Learning for Clinical Decision Support* (D. Stoyanov, Z. Taylor, G. Carneiro, T. Syeda-Mahmood, A. Martel, L. Maier-Hein, J. M. R. Tavares, A. Bradley, J. P. Papa, V. Belagiannis, J. C. Nascimento, Z. Lu, S. Conjeti, M. Moradi, H. Greenspan, and A. Madabhushi, eds.), (Cham), pp. 155–164, Springer International Publishing, 2018.

[84] V. Kearney, B. P. Ziemer, A. Perry, T. Wang, J. W. Chan, L. Ma, O. Morin, S. S. Yom, and T. D. Solberg, “Attention-aware discrimination for MR-to-CT image translation using cycle-consistent generative adversarial networks,” *Radiology: Artificial Intelligence*, vol. 2, no. 2, p. e190027, 2020.

[85] J. Zhao, D. Li, Z. Kassam, J. Howey, J. Chong, B. Chen, and S. Li, “Tripartite-GAN: Synthesizing liver contrast-enhanced MRI to improve tumor detection,” *Medical Image Analysis*, vol. 63, p. 101667, 2020.

[86] Z. Yuan, M. Jiang, Y. Wang, B. Wei, Y. Li, P. Wang, W. Menpes-Smith, Z. Niu, and G. Yang, “Sara-GAN: Self-attention and relative average discriminator based generative adversarial networks for fast compressed sensing MRI reconstruction,” *Frontiers in Neuroinformatics*, vol. 14, p. 58, 2020.

[87] M. Li, W. Hsu, X. Xie, J. Cong, and W. Gao, “Sacnn: Self-attention convolutional neural network for low-dose CT denoising with self-supervised perceptual loss network,” *IEEE Transactions on Medical Imaging*, vol. 39, no. 7, pp. 2289–2301, 2020.

[88] Y. Xie, J. Zhang, C. Shen, and Y. Xia, “Cotr: Efficiently bridging cnn and transformer for 3d medical image segmentation,” 2021.

[89] S. A. Kamran, K. F. Hossain, A. Tavakkoli, S. L. Zuckerbrod, K. M. Sanders, and S. A. Baker, “VtGAN: Semi-supervised retinal image synthesis and disease prediction using vision transformers,” 2021.

[90] H.-C. Shin, A. Ihsani, S. Mandava, S. T. Sreenivas, C. Forster, J. Cha, and A. D. N. Initiative, “GANbert: Generative adversarial networks with bidirectional encoder representations from transformers for MRI to PET synthesis,” 2020.

[91] X. Zhang, X. He, J. Guo, N. Ettehadi, N. Aw, D. Semanek, J. Posner, A. Laine, and Y. Wang, “Ptnet: A high-resolution infant MRI synthesizer based on transformer,” 2021.

[92] D. Karimi, S. Vasylechko, and A. Gholipour, “Convolution-free medical image segmentation using transformers,” 2021.

[93] Y. Dai and Y. Gao, “Transmed: Transformers advance multi-modal medical image classification,” 2021.

[94] B. H. Menze, A. Jakab, S. Bauer, J. Kalpathy-Cramer, and et al., “The multimodal brain tumor image segmentation benchmark (brats),” *IEEE Transactions on Medical Imaging*, vol. 34, no. 10, pp. 1993–2024, 2015.

[95] S. Bakas, H. Akbari, A. Sotiras, M. Bilello, M. Rozycski, J. Kirby, J. Freymann, K. Farahani, and C. Davatzikos, “Advancing the cancer genome atlas glioma MRI collections with expert segmentation labels and radiomic features,” *Nature Scientific Data*, vol. 4, p. 170117, 2017.

[96] S. Bakas, M. Reyes, A. Jakab, S. Bauer, M. Rempfler, A. Crimi, R. T. Shinohara, C. Berger, and et al., “Identifying the best machine learning algorithms for brain tumor segmentation, progression assessment, and overall survival prediction in the brats challenge,” 2019.

[97] T. Nyholm, S. Svensson, S. Andersson, J. Jonsson, M. Sohlin, C. Gustafsson, E. Kjellén, K. Söderström, P. Albertsson, L. Blomqvist, B. Zackrisson, L. E. Olsson, and A. Gunnlaugsson, “MR and CT data with multiobserver delineations of organs in the pelvic area—part of the gold atlas project,” *Medical Physics*, vol. 45, no. 3, pp. 1295–1300, 2018.

[98] M. Jenkinson and S. Smith, “A global optimisation method for robust affine registration of brain images,” *Medical Image Analysis*, vol. 5, pp. 143–156, 2001.

[99] H. Lan, the Alzheimer Disease Neuroimaging Initiative, A. W. Toga, and F. Sepehrband, “Three-dimensional self-attention conditional GAN with spectral normalization for multimodal neuroimaging synthesis,” *Magnetic Resonance in Medicine*, vol. 86, no. 3, pp. 1718–1733, 2021.

[100] D. P. Kingma and J. Ba, “Adam: A method for stochastic optimization,” in *3rd International Conference on Learning Representations, ICLR 2015, San Diego, CA, USA, May 7-9, 2015, Conference Track Proceedings* (Y. Bengio and Y. LeCun, eds.), 2015.

[101] T. Ridnik, E. Ben-Baruch, A. Noy, and L. Zelnik-Manor, “Imagenet-21k pretraining for the masses,” 2021.

[102] Z. Wang, A. Bovik, H. Sheikh, and E. Simoncelli, “Image quality assessment: From error visibility to structural similarity,” *IEEE Transactions on Image Processing*, vol. 13, pp. 600 – 612, 05 2004.

[103] Z. Wojna, V. Ferrari, S. Guadarrama, N. Silberman, L. chieh Chen, A. Fathi, and J. Uijlings, “The devil is in the decoder: Classification, regression and GANs,” *IJCV*, 2019.

[104] R. Durall, M. Keuper, and J. Keuper, “Watch your up-convolution: Cnn based generative deep neural networks are failing to reproduce spectral distributions,” in *2020 IEEE/CVF Conference on Computer Vision and Pattern Recognition (CVPR)*, pp. 7887–7896, 2020.

[105] J. Deng, W. Dong, R. Socher, L.-J. Li, K. Li, and L. Fei-Fei, “Imagenet: A large-scale hierarchical image database,” in *2009 IEEE Conference on Computer Vision and Pattern Recognition*, pp. 248–255, 2009.

[106] P. Foret, A. Kleiner, H. Mobahi, and B. Neyshabur, “Sharpness-aware minimization for efficiently improving generalization,” 2021.

[107] I. Tolstikhin, N. Houlsby, A. Kolesnikov, L. Beyer, X. Zhai, T. Unterthiner, J. Yung, A. Steiner, D. Keysers, J. Uszkoreit, M. Lucic, and A. Dosovitskiy, “Mlp-mixer: An all-mlp architecture for vision,” 2021.

[108] S. Zhai, W. Talbott, N. Srivastava, C. Huang, H. Goh, R. Zhang, and J. Susskind, “An attention free transformer,” 2021.